Insight into the Directional Thermal Transport of Hexagonal Boron Nitride Composites

M. Hamidinejad, A. Zandieh, J.H. Lee, J. Papillon, B. Zhao, N. Moghimian, E. Maire, T. Filleter, C.B. Park

An Insight into the Directional Thermal Transport of Hexagonal Boron Nitride Composites

Mahdi Hamidinejad [a], Azadeh Zandieh [a], Jung Hyub Lee [a], Justine Papillon [b], Biao Zhao [a], Nima Moghimian [c], Eric Maire [b], Tobin Filleter [a], and Chul B. Park [a]**

[a] Department of Mechanical and Industrial Engineering, University of Toronto, 5 King's College Road, Toronto, Canada M5S 3G8

[b b] University of Lyon, INSA de Lyon, MATEIS UMR CNRS 5510, Bât. Saint Exupery, 23 Av. Jean Capelle, F-69621 Villeurbanne, France

[c] NanoXplore Inc., 25 Boul. Montpellier, Saint-Laurent, QC, H4N 2G3

*Corresponding Authors' Information: E-mail: filleter@mie.utoronto.ca; park@mie.utoronto.ca
Address: 5 King's College Road, Toronto, Ontario M5S 3G8, Canada*

Abstract:

Ideal dielectric materials for microelectronic devices should have high directionally-tailored thermoconductivity with low dielectric constant and loss. Hexagonal boron nitride (hBN) with excellent thermal and dielectric properties shows promise for fabrication of thermoconductive dielectric polymer composites. Herein, a simple method for fabrication of lightweight polymer/hBN composites with high directionally-tailored thermoconductivity and excellent dielectric properties is presented. The solid polymer/hBN composites are manufactured by melt-compounding and injection molding. The porous composites are successfully manufactured in an injection molding process through supercritical fluid (SCF) foaming. X-ray tomography provides direct visualization of the internal microstructure and hBN orientation leading to an in-depth understanding of the directionally-dependent thermoconductivity of the polymer/hBN composites. Shear-induced orientation of hBN platelets in the solid HDPE/hBN composites leads to significant anisotropic thermal conductivity. The solid HDPE/23.2 vol.% hBN composites show an in-plane thermoconductivity as high as 10.1 W $m^{-1} K^{-1}$ while the through-plane thermoconductivity is limited to 0.28 W $m^{-1} K^{-1}$. However, the generation of a porous structure via SCF foaming imparts in situ exfoliation, random orientation and interconnectivity of hBN

platelets within the polymer matrix. This results in highly isotropic thermoconductivity with higher bulk thermal conductivity in the lightweight porous composites as compared to their solid counterparts. Furthermore, the electrically insulating composites developed in this study exhibit low dielectric constant and ultralow dielectric loss. Thus, this study presents a simple fabrication method to develop lightweight dielectric materials with tailored thermal conductivity for modern electronics.

Keywords: Porous Polymer/hexagonal Boron Nitride, Isotropic and Anisotropic Thermal Conductivity, Dielectric Properties, Microcellular Foaming, X-ray Tomography

1. Introduction

For decades, continuous miniaturization and high-power densification have been the hallmark of microelectronic device development [1]. However, overheating is often the greatest barrier to further miniaturization due to high functional and power density requirements [1,2]. Thus, effective heat dissipation is crucial to guarantee optimal performance and extend the service life of microelectronic devices [2,3]. Efficient materials for heat management in microelectronics should offer high thermoconductivity, low dielectric constant (ε') and low dielectric loss ($tan\ \delta$) [4]. Low ε' and low $tan\ \delta$ can efficiently slow down the crosstalk and capacitative coupling in high operation speed microelectronic devices, and thereby decrease the resistance-capacitance delay effect [4,5].

Some ceramics offer high thermoconductivity and a perfect combination of electrical properties; however, their processing is highly challenging [6]. Polymers are easy to process and have excellent dielectric properties, however, polymers suffer from low thermal conductivity (ranging from 0.2 to 0.4 W m^{-1} K^{-1}) [7]. Therefore, ceramic-based polymer composites can offer an excellent combination of properties, including processability, relatively high thermoconductivity, electrical insulation, low ε' and low $tan\ \delta$. This combination of properties has shown great promise for using

ceramic-based polymer composites as heat dissipation components in microelectronic packaging, and light emitting diodes [6].

Various ceramic fillers such as silicon carbide [8], boron nitride [6,9–11], aluminum oxide (Al_2O_3) [7], and aluminum nitride (AlN) [12] have been utilized to enhance the thermal conductivity of polymers. Polymer composites that include Al_2O_3 and AlN offer high thermoconductivity and electrical insulation. Nonetheless, they usually have high ε' and high *tan δ*. In addition, ceramic fillers with low ε' and low *tan δ*, such as SiO_2, fail to efficiently improve the thermoconductivity of polymers [6–8,13].

On the other hand, hBN, a two-dimensional material with sp^2 covalent bonds [14], with excellent thermoconductivity (in-plane thermoconductivity ~600 W m^{-1} K^{-1}) [11] and very high thermal and chemical stability [14], shows promise for fabrication of thermally conductive dielectric materials. Moreover, hBN has a wide bandgap energy (direct and indirect energies of hBN have been reported as high as 7.1 eV [15]) and low ε' (3~5) [16]. Therefore, it is expected that polymer composites with hBN will offer a combination of high thermoconductivity, low electrical conductivity, low ε' and low *tan δ*, as required for microelectronic packaging [6,10,11,17]. However, the thermoconductivity of polymer composites is greatly influenced by various parameters such as the interfacial thermal resistance, interfacial phonon scattering [3,18], orientation, dispersion and type of additives used in the polymeric matrix [3,10,11,17]. Despite the high thermoconductivity of hBN platelets, the thermoconductivity of existing polymer/hBN composites is extremely limited due to the challenges involved in the exfoliation/dispersion [19–21] and hBNs' orientation [10,11,17] within the polymer matrix.

Various techniques such as alignment of hBN platelets by a magnetic field [10,11,22], synergy effects of size and shape of hBN particulates [23], in situ polymerization [17,24,25], exfoliation and functionalization of hBN platelets [19,26] and the use of hybrid additives [27,28] have been used to

enhance and control the directionality of thermal transport in the polymer/hBN composites. Nonetheless, most of the fabrication methods for polymer/hBN composites, including the foregoing studies, are batch-type techniques which are time consuming, expensive and hardly scalable.

However, melt compounding and injection molding of polymer/hBN composites can offer a continuous fabrication route. When injection molding is combined with supercritical fluid (SCF) foaming, a porous structure can be created. This can improve the design flexibility to address various functionalities for different applications [3,29–34]. SCF foaming can increase the level of dispersion [32,35] and exfoliation [3,36,37] of fillers in the polymer matrix. Furthermore, shear-induced orientation of filler through a conventional injection molding process [3,30] and the orientation and alignment of fillers developed by cellular growth in foaming [3,30,31,35] can, respectively, offer anisotropic [3] and isotropic thermoconductivity [3,4]. It is also believed that achieving low k ($2.5< \varepsilon'<3$) and ultralow k ($\varepsilon'<2.2$) materials is not possible without embracing the concept of porosity [5]. Therefore, the challenging fabrication procedure for efficient dielectric polymer/hBN composites with tailored thermal conductivity (isotropic and anisotropic) can be facilitated with injection molding and physical foaming. Given the importance of fillers' orientation on functional properties of polymer composites, an accurate, nondestructive three-dimensional (3D) inspection of internal structure becomes increasingly critical. X-ray tomography is one possible method that can be used to assess the internal microstructures of polymer composites to fundamentally understand their structure-functional properties relationships. This method is a non-destructive testing technique developed from the medical field. It can provide sectional or 3D representations of the internal structure of the polymer composites [38,39].

Herein, a simple method of fabrication of solid and porous high-density polyethylene (HDPE)/hBN composites with high thermoconductivity, low ε' and ultralow $tan\ \delta$ is presented. X-

ray tomography, for the first time provided a clear analysis of the internal structures and hBN's orientation. This led to a complete understanding of the anisotropic versus isotropic behavior as well as the enhancements in the thermoconductivity of the polymer/hBN composites. The study revealed that the shear-induced orientation of hBN platelets in solid injection molded samples resulted in primarily anisotropic thermal conductivity. Using this fabrication method, the in-plane thermoconductivity reached 10.11 W m^{-1} K^{-1}, while the through-plane thermoconductivity was limited to 0.28 W m^{-1} K^{-1} for HDPE/23.2 vol.% hBN composites. On the contrary, it was also demonstrated that the generation of 10% porous structure can result in high level of isotropic thermal conductivity with high bulk thermal conductivity, as compared to solid samples. For instance, the bulk thermal conductivity of solid and porous HDPE/23.2 vol.% hBN composites was 1.73±0.01 and 2.07±0.04, respectively. The porous structure changed the orientation and arrangement of hBN platelets and enhanced their interconnectivity, and exfoliation/dispersion in the polymer matrix. In addition, the introduction of a porous structure developed through SCF foaming decreased ε' and *tan* δ of the hBN-based polymer composites.

2. Results and Discussion

2.1. Microstructure and Morphology of Polymer/hBN Composites

The X-ray tomography images of HDPE/hBN (**Figure 1**a**)** clearly show the internal microstructure and the orientation and arrangement of hBN platelets in the solid and porous HDPE/hBN composites. The solid samples have completely solid structures. Two clear regions including skin (~1.2 mm on each side) and the core were observed in the solid injection molded samples. The hBN platelets in the skin region of solid samples were orientated in the injection direction (flow direction). The shear-induced orientation of hBN is generated due to the applied high shear rate during the injection process. The alignment of fillers due to the high shear rate in

the injection molded polymeric composites has been frequently studied in literature [3,30,40]. On the other hand, the hBN platelets in the core region of the solid injection molded composites follow the fountain flow orientation. The X-ray image shows a clear transition of hBNs' orientation from highly oriented in the skin region to curved and even perpendicular to the flow direction in the core region.

The porous HDPE/hBN composites had non-homogeneous microcellular structure with average cell size of 5.8 ± 3.7 μm in the skin region and 9.5 ± 5.6 μm in the core region (more details on the cell size of the porous composites is presented in Supporting Information; Section S1 (**Figure S1**)). The non-homogeneous cell morphology was due to the dispersed hBN platelets acting as heterogeneous nucleating sites for cells [41].

The cellular growth in the porous samples changed the orientation of hBN platelets and rearranged them around the growing cells [3,29]. This enhanced the chance of interconnectivity of hBN platelets and hBN-hBN contact. As shown in Figures 1c-1d, the generation of porosity significantly increased the size of interconnected clusters of hBN platelets; particularly through the thickness direction (Z direction) of the composites. This shows the effectiveness of the microcellular structure in increasing the interconnectivity of hBN platelets. By increasing the concentration of hBN platelets, the effectiveness of the porosity in improving the interconnectivity of the hBN platelets becomes more pronounced as shown in **Figure S2**.

To quantitatively investigate the microstructure and the hBN orientation in solid and porous samples, the X-ray tomography images were processed in the form of extracted slices. Figure 1b shows relative and cumulative frequencies of hBN platelet orientation with respect to the flow direction at different depths from the skin surface. For each X-ray tomography image, 100-200 hBN platelets were taken into consideration to quantify hBN orientation by measuring the angle of hBN platelets in the considered plane of observation by Fiji freeware.

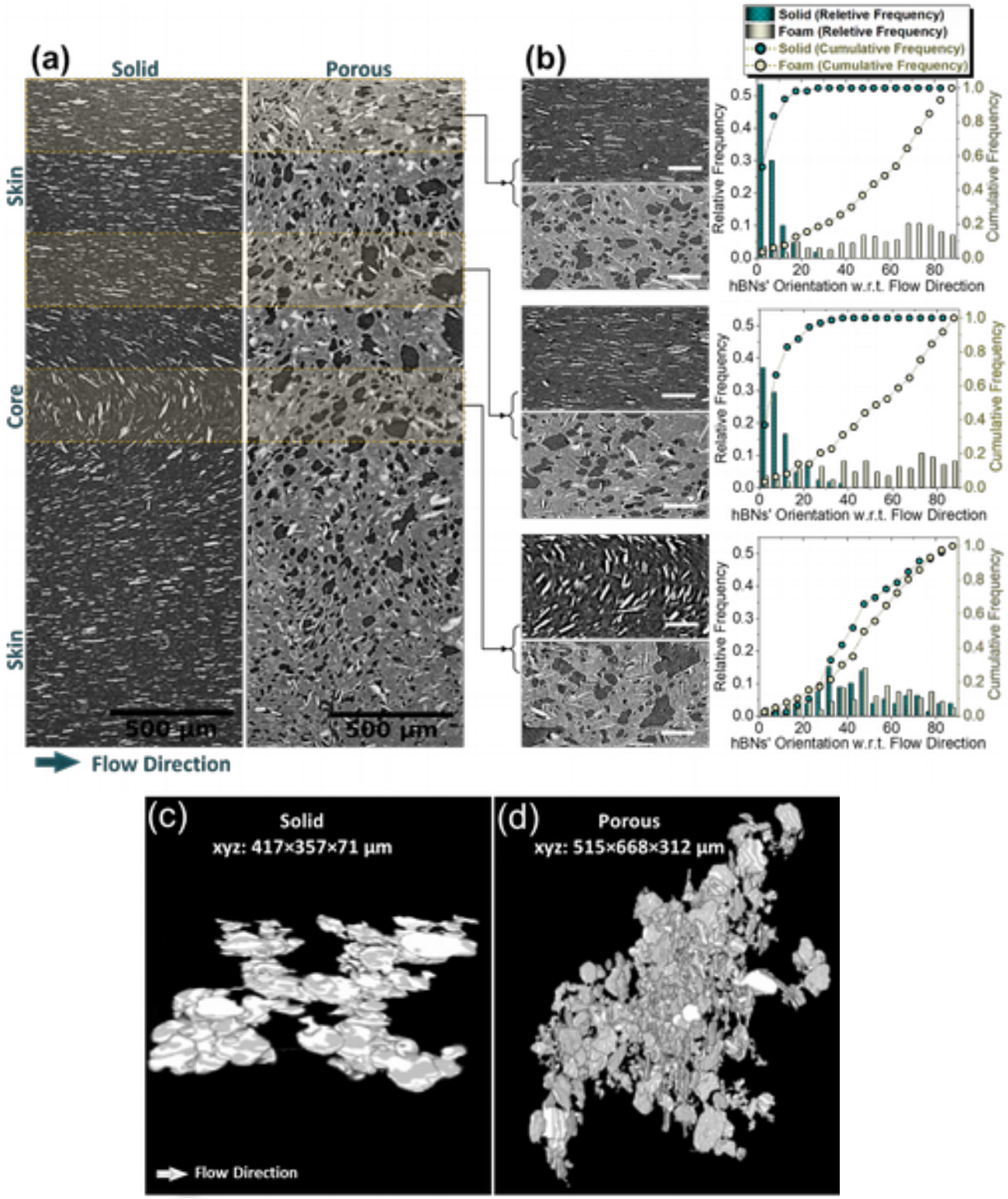

Figure 1. (a) Representative X-Ray tomography of solid and porous (20% porosity) HDPE/10.2 vol.% hBN composite over the whole thickness; Scale bars are 500 µm; (b) statistical analysis of hBN orientation in the solid and porous HDPE/10.2 vol.% hBN composites; scale bars are 100 µm. Representative 3D X-Ray tomography of the biggest interconnected clusters of hBN platelets in (c) the solid; (d) and the porous HDPE/10.2 vol.% hBN composites. Z represents the thickness direction of samples.

In the skin region close to the sample surface (~0-300μm depth), the hBN platelets in the solid composites were highly oriented in the direction of flow. For instance, 98% of hBN platelets in solid HDPE/hBN composites had orientations with less than 20 degrees deviation with respect to the flow direction. This shows an ultra-high level of hBN orientation in the skin of solid samples. However, in the porous samples, the distribution of hBN platelet orientation was uniform, and cumulative frequency of hBN platelet orientation with respect to the flow direction gradually increased, indicating their random orientation in the composite.

In the skin region closer to the core region (~600μm-900μm depth), the hBN platelets were still highly oriented in the solid samples, and 92% of them were orientated with only slight deviation (<20 degrees) from the flow direction. Nevertheless, at the same depth, uniform distribution of hBN platelet orientation in the porous HDPE-hBN composites suggests a high level of isotropic orientation of filler in the polymer matrix.

In the core region, the distribution of hBN platelet orientation in the solid samples became more uniform as compared to the skin region, which is indication of their relatively random orientation in the core region due to fountain flow-induced orientation of hBN platelets. The hBN platelets maintained their random orientation in the core region of porous samples.

The isotropic orientation of hBN platelets in both regions (skin and core) of porous samples can be mainly related to (i) lower viscosity of HDPE/hBN due to the dissolution of supercritical N_2 and (ii) the cellular growth during foaming. The growth of cells rearranged and dislocated the hBN platelets. This changed the hBN shear-induced orientation and, thereby, increased the chance of hBN platelet interconnections [40].

X-ray diffraction (XRD) was conducted to further characterize the exfoliation/dispersion of HDPE/hBN composites. **Figure 2**a shows the XRD patterns for neat HDPE and solid and porous

HDPE/10.2 vol.% hBN composites. The 2θ = 26.6° is the diffraction peak of (002) planes in hBN crystals which is associated with interlayer distance of monolayer hBN sheets. Based on the Bragg's law, the hBN (002) plane distance was 0.345 nm. It is notable that the intensity of (002) diffraction of solid HDPE-hBN significantly decreased after SCF foaming (inset Figure 2a). This reduction in the intensity of the (002) diffraction peak can be related to further exfoliation and/or dispersion of hBN in the polymer matrix [42–44]. Furthermore, it is possible to identify the orientation of hBN platelets by monitoring the intensity of the (002) and (100) diffraction peaks simultaneously [10,11].

As shown in Figure 1, the orientation of hBN platelets are responsible for change in the intensity of the (002) and (100) peaks[10,11]. In the inset to Figure 2a, it is notable that the (100) diffraction peaks of the porous samples exhibited slightly stronger intensity as compared to those of solid samples. This firstly suggests that the hBN platelets were highly oriented on the surface of the solid samples, while the hBN platelets in the porous samples had less shear-induced orientation due to the presence of a weak (100) diffraction peak [10,11,45] (which is in good agreement with Figure 1). Secondly, the reduced intensity of (002) diffraction peaks in the porous samples can be partially resulted from random orientation of hBN and partially by further exfoliation of hBN platelets. The latter conclusion was drawn since the significant reduction in the (002) intensity of the porous samples resulted in a very small increase in the (001) intensity. Therefore, the reduced (002) intensity can be partially related to the further exfoliation of hBN.

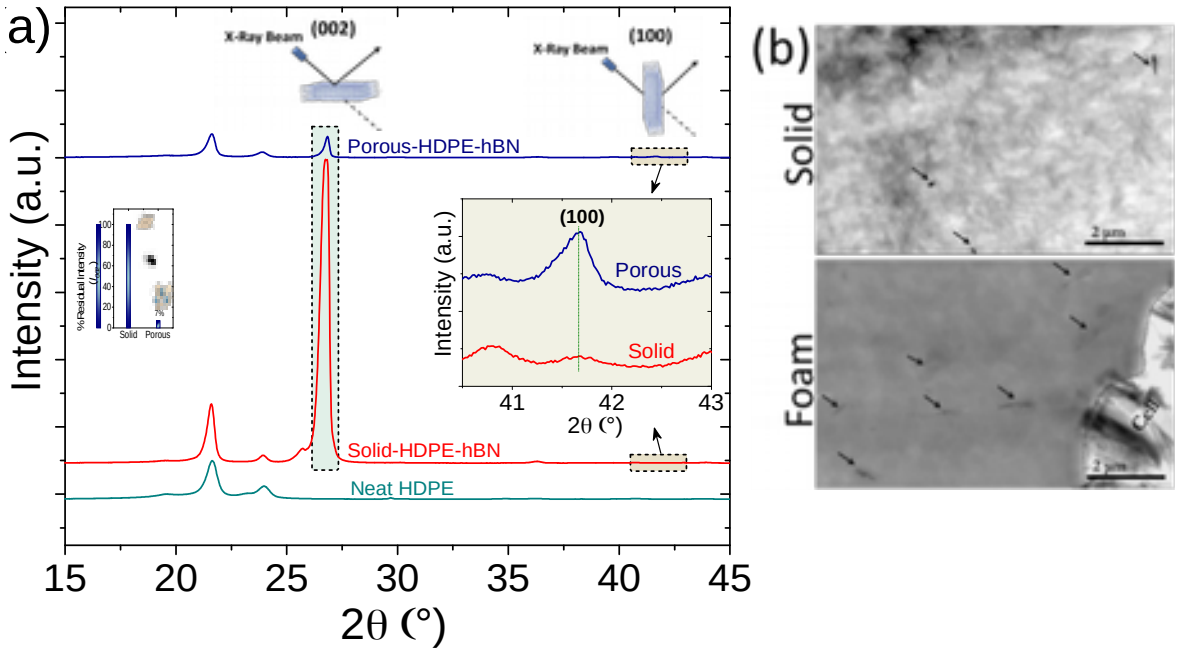

Figure 2. (a) XRD spectra of neat HDPE, and solid and porous HDPE/10.2 vol.% hBN; (b) representative TEM of the solid and porous HDPE/10.2 vol.% hBN. Porous samples have 10% porosity. The arrows point to the hBN platelets in the polymer/hBN composites.

Figures 2b, shows representative TEM of the solid and porous (10% porosity) HDPE/hBN composites. There are thinner layers and higher number of hBN platelets in the porous composites as compared to their solid counterparts indicating efficient exfoliation/dispersion of hBN platelets via SCF-foaming. When the HDPE/hBN mixture is treated with SCF under high pressure (~24 MPa) while the act of shearing in the injection process is being applied, the SCF can defuse between the layers of hBN. During the mixture injection into the mold the SCF undergoes phase transformation as a result of rapid depressurization. The transformation of SCF into the gaseous state can exfoliate and disperse the hBN layers [3,46]. Furthermore, the nucleated cells and their growth near the hBN can further disperse the hBN platelets within the polymer matrix [3,36].

2.2. Thermal Conductivity

2.2.1. Bulk Thermal Conductivity

Figure 3a shows how the bulk thermoconductivity of the solid and porous HDPE/hBN composites varies as a function of the hBN concentration. In this work, the volume percentage of hBN platelets was reported with regard to the total volume of porous polymer/hBN composites, considering both gaseous and solid phases. In all the solid and porous samples, the thermoconductivity of the HDPE/hBN composites was highly dependent on the hBN content. The generation of porous structure in the HDPE/hBN composites also significantly affected their thermal conductivity. The incorporation of 10% porosity decreased the bulk thermal conductivity of HDPE/hBN composite containing 4.8, 7.5, 10.2 and 13 vol.% hBN. However, the bulk thermal conductivities of the porous HDPE/hBN composite (with 10% porosity) started to outperform those of the solid composites at hBN loadings of more than 13 vol.%. As shown in Figure S2, at a higher hBN content (>13 vol.%), there is enough hBN within the polymer matrix to be interconnected due to foaming action and to form thermo-conductive paths in the 3D bulk of the composite. However, at a lower hBN content (<13 vol.%), the hBN platelets are too far from each other to fully percolate over the whole bulk of composites, even though they are randomly oriented and more interconnected as compared to the solid samples (Figures 1c and 1d). In other words, below a loading of 13 vol.% hBN, polymer mediated between the hBN platelets and prevented direct hBN-hBN contact, leading to higher interfacial thermal resistance due to phonon scattering [4,47,48]. For instance, the incorporation of 10% porosity increased the average bulk thermal conductivity of the HDPE/23.2 vol.% hBN composites from 1.73±0.01 $Wm^{-1}K^{-1}$ to 2.07±0.04 $Wm^{-1}K^{-1}$.

Although the incorporation of a small amount of porosity (10%) enhanced the bulk thermoconductivity of the polymer/hBN composites, increasing the porosity to 20% was

ineffective due to the increased insulation contribution of the voids. As is notable in Figure 3a, for all hBN contents, the bulk thermal conductivity of porous HDPE/hBN composite containing 20% porosity was lower than their solid and 10% porosity porous counterparts. This can be attributed to the competing relationship between the ultralow thermoconductivity of the voids and random orientation of hBN induced by foaming. An excessive degree of porosity (that is, 20%) resulted in more voids within the composites, leading to a lower bulk thermal conductivity.

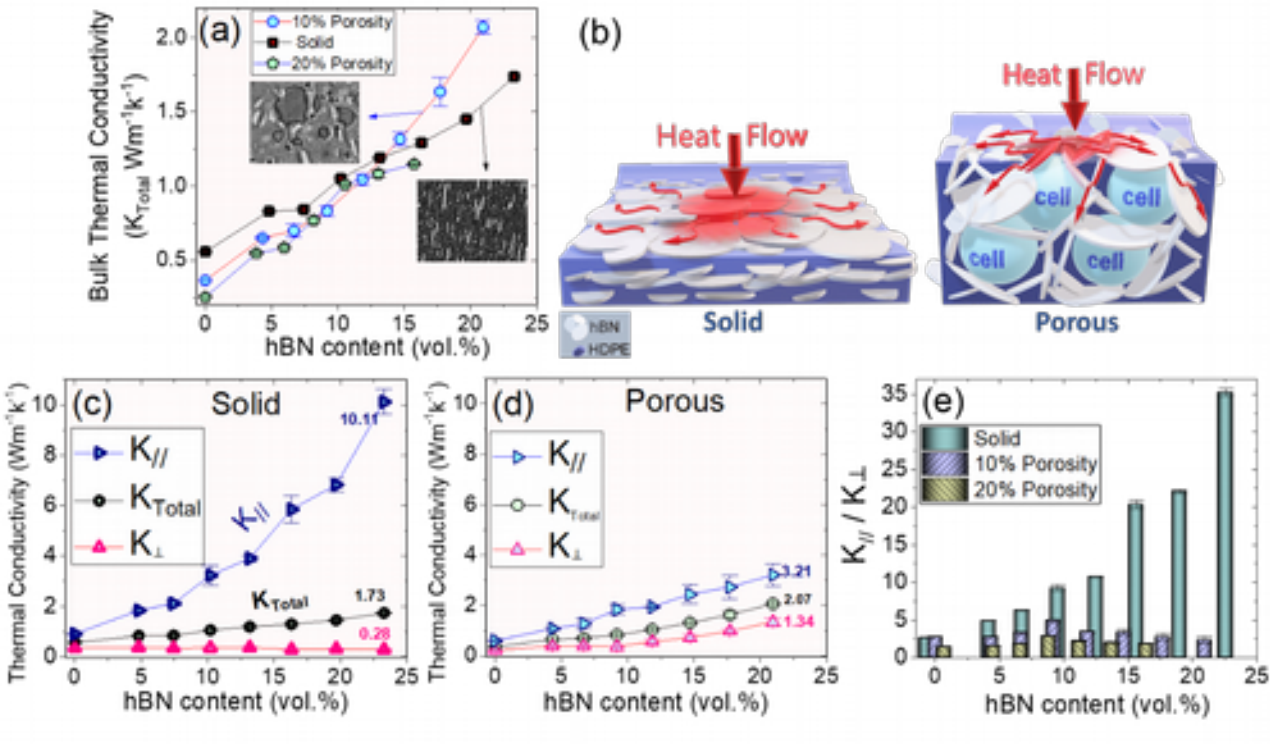

Figure 3. (a) The bulk thermal conductivity (K_{total}) of solid and porous HDPE/hBN composites. (b) Schematic representation of anisotropic and isotropic heat dissipation in solid and porous composites. In-plane and through-plane thermoconductivities of the (c) solid and (d) porous samples (10% porosity). (e) The $K_{//}/K_{\perp}$ ratio as a measure of anisotropy of the thermal conductivity for the solid and porous samples.

Briefly, the generation of an optimum porosity level (10%) changed the skin-core morphology of the solid composites and enhanced the local interconnection of the hBN platelets, while the insulating effect of voids was minimized. The enhanced bulk thermoconductivity of the HDPE/hBN composites with a small amount of porosity (10%) can be mainly attributed to: (i)

change of the shear-induced orientation of hBN into random orientation due to cellular growth; (ii) enhanced level of local interconnectivity of hBN platelets within the bulk of the composite; (iii) higher level of hBN dispersion/exfoliation in the polymer matrix. Figure 3b schematically shows the heat dissipation in the solid and porous composites.

2.2.2. Directional Thermal Conductivity; Anisotropic versus Isotropic

Figures 3c and 3d show the in-plane (//), through-plane (⊥) and bulk thermal conductivity of HDPE/hBN composites. As shown in Figure 3c, the in-plane thermal conductivity ($K_{//}$) of the solid HDPE/hBN composites sharply increased with an increased hBN loading, while the through-plane thermal conductivity ($K_{\perp}$) remained almost constant. For instance, the $K_{//}$ of the solid HDPE/23.2 vol.% hBN composites reached 10.1±0.5 $Wm^{-1}K^{-1}$, which is about 36 times higher than their $K_{\perp}$.

This can be attributed to the high level of in-plane orientation of the hBN platelets in ~80% of the solid sample thickness, as discussed earlier (Figure 1). The in-plane alignment of hBN platelets can form numerous in-plane thermally conductive paths where phonons can be transferred through hBN-hBN interfaces with low interfacial thermal resistance. However, along the perpendicular direction, the thermoconductive hBN-hBN pathways are insulated by layers of polymer matrix. Therefore, phonon transfer through-plane will be highly limited due to high interfacial thermal resistance of polymer-hBN, resulting in ultrahigh anisotropic thermal conductivity [47]. Nonetheless, anisotropic thermal conductivity can decrease the 3D bulk thermal conductivity within such composites [4].

The physical foaming, on the other hand, developed isotropic thermoconductivity within the HDPE/hBN composites. Microcellular foaming considerably increased the through-plane thermoconductivity of HDPE/hBN composites and decreased the in-plane thermoconductivity, which resulted in higher bulk thermal conductivity with a significant level of isotropy. For

example, physical foaming increased the through-plane thermoconductivity of the solid HDPE/23.2 vol.% hBN composites by 478.5%, while their in-plane conductivity decreased by 68.2%. The through-plane and in-plane thermoconductivities of porous HDPE/hBN composites containing 10% and 20% porosity, as compared to solid counterparts, are presented as a function of the hBN content in **Figure S3**.

Figure 3e demonstrates the ratio of in-plane to through-plane thermal conductivity ($K_{//}/K_{\perp}$) of the HDPE/hBN as a function of filler loading. The $K_{//}/K_{\perp}$ of the solid HDPE/hBN rapidly increased with an increased hBN content. This shows the significant impact of hBN platelet orientation and their in-plane interconnection on the ultrahigh in-plane thermoconductivity and ultralow through-plane thermoconductivity of the solid composites. However, after the introduction of foaming, the $K_{//}/K_{\perp}$ ratio was almost independent of hBN content, suggesting the significant impact of random orientation of hBN platelets and their 3D interconnection on the isotropic thermoconductivity of porous HDPE/hBN composites. By increasing the porosity to 20% the $K_{//}/K_{\perp}$ was further reduced, which resulted in a higher level of isotropic thermal conductivity.

Figure S4 shows Differential Scanning Calorimetry (DSC) measurements on the HDPE/hBN composites. It is notable that the crystallinity and melting point of the HDPE in the HDPE/hBN composites are not affected by foaming or by the hBN loading due to the fast crystallization kinetics of high-density polyethylene which might not be influenced by the investigated processing parameters in this study. Hence, the effect of crystallinity on the thermoconductivity of composites is considered negligible in this work.

2.3. Dielectric Properties of HDPE-hBN Composites

In addition to high thermoconductivity, a dielectric material for modern electronics should also offer low dielectric constant (ε') and low dielectric loss ($tan\ \delta$). Generally, the dielectric

permittivity is defined as a complex function as: $\varepsilon(\omega) = \varepsilon'(\omega) - i\varepsilon''(\omega)$, where, ω is the frequency and $\varepsilon'(\omega)$ and $\varepsilon''(\omega)$ are, respectively, the real and the imaginary parts of the dielectric permittivity [49]. The real permittivity (dielectric constant, ε') is attributed to displacement of the charges within the material governed by different types of polarization. Generally, below 1 MHz, the most dominant type of polarization is interfacial polarization [49]. Imaginary permittivity (ε'') is the measure of energy loss and used to quantify *tan δ*. The ratio of ε'' to ε' is defined as *tan δ* [31]. *tan δ* in polymeric composites is mainly governed by ohmic and polarization loss [50].

Figures 4a and 4b show ε' of the solid and porous HDPE/hBN composites across a frequency range from 1Hz to 1×10^{-5}, respectively. The real permittivity of all samples (solid and porous) is nearly frequency-independent, which is the characteristics of electrically insulative polymeric composites [51]. The real permittivity of neat HDPE very slightly increased from 2.91 to 3.00±0.04 with incorporation of 23.2 vol.% hBN in the solid HDPE/hBN composites. This can be related to the similar values of ε' for HDPE (i.e. ε' =2.91) and hBN platelets (i.e. ε' =3.76 [16]). According to the Maxwell–Wagner–Sillars (MWS) effect [49], in polymeric composites interfacial polarization occurs due to a considerable contrast between the permittivity and/or electrical conductivity of the filler and the polymer. Therefore, the interfacial polarization in the solid HDPE/hBN composites is expected to be very limited, since the HDPE and hBN platelets possess the same level of ε' and the same electrical conductivity.

The development of a porous structure within the composites can lower ε' of materials [4,52,53]. As shown in Figure 4b, the introduction of 10% porosity through microcellular foaming marginally decreased ε' of HDPE/hBN composites (7%-13%). This can be attributed to the low dielectric constant of air (i.e. ε' =1) [54].

As seen in Figures 4c and 4d, *tan δ* of the neat HDPE increased with the increase in hBN content, however, the values of *tan δ* were still very low and ranged between 0.0025 to maximum 0.0068

at 100 Hz for various solid and porous HDPE/hBN composites. The ultralow *tan δ* of the HDPE/hBN composites is related to their ultralow ohmic loss, which is originated from high electrical resistivity of composites [55,56], as shown in Figures 4e and 4f. In addition to the ohmic loss, *tan δ* can also be affected by polarization loss [49]. However, in the composite system studied in this work, the polarization loss is very limited due to very low *ε′*.

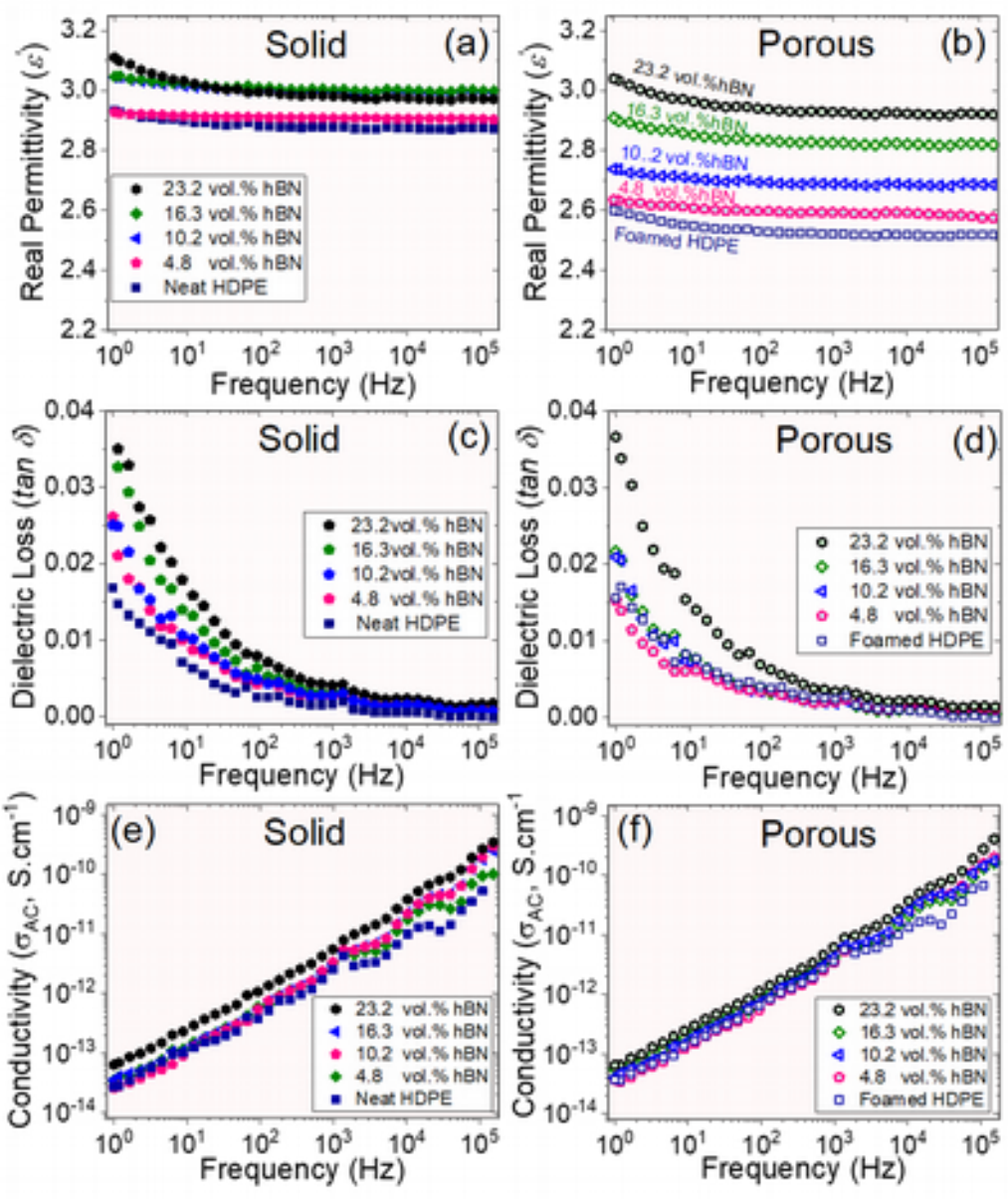

Figure 4. *ε′* of (a) the solid, and (b) porous HDPE/hBN composites. *tan δ* of (c) the solid, and (d) porous HDPE/hBN composites. The electrical conductivity of (e) the solid, and (f) porous (10% porosity) HDPE/hBN composites.

Figures 4e and 4f show the electrical conductivity of the HDPE/hBN composites over 1 Hz to $1\times10^{+5}$ Hz. The electrical conductivity of all the composites (solid and porous) followed a frequency-dependent behavior over 1 Hz to $1\times10^{+5}$ Hz. This behavior is a typical characteristic of insulative polymer composites [57,58]. This can be related to the ultrahigh electrical resistivity of the polymer matrix and the hBN platelets (with wide bandgap energy [15]). Therefore, the electrical conductivity of the fabricated composites is almost the same as neat HDPE.

Table 1 shows the summary of this work as compared to some of the recent advances in manufacturing of thermoconductive dielectric polymer/hBN composites. Most of the listed studies require complicated synthesis procedures to develop directionally-tailored thermoconductivity. These methods are hardly scalable with high material cost due to the use of boron nitride nanosheets (BNNS). In particular, Yuan et al. [59] self-assembled the BNNS and FeCo nanocubes by controlling the polarity of the fillers. Subsequently, the complex nanomaterials (BNNS + FeCo) were oriented using magnetic field to develop anisotropic thermal conductivity. They achieved a thermoconductivity of 2.25 W m^{-1} K^{-1} for the composite with 50 wt. % BNNS and 30 wt. % FeCo. Han et al. [60] fabricated an anisotropic thermally conductive, nacre-mimetic epoxy/BNNS composite. They reported high level of anisotropic thermal conductivity with a $K_{//}$ / $K_{\perp}$ ratio as high as 12. They achieved the in-plane thermoconductivity of 6.07 W m^{-1} K^{-1} at 15 vol % BNNS loading. Chen et al. [47] developed polyvinylidene fluoride (PVDF)/BNNS composite by electrospinning. They reported a high in-plane thermoconductivity of 16.3 W m^{-1} K^{-1} at 33 wt.% BNNS loading with a high level of the anisotropic thermoconductivity ($K_{//}$ /$K_{\perp}$ ratio as high as 21). Lin et al. [11] used hBN platelets to fabricate anisotropic thermoconductive polymer/hBN composites. They modified the surface of hBN platelets with iron oxide and used a magnetic field to align the modified hBN. Morishita and Okamoto [19] presented a direct exfoliation method for hBN using superacid. They developed soluble functionalized BNNS with chlorosulfonic acid and

randomly dispersed them in polybutylene terephthalate. They achieved a through-plane thermoconductivity of 0.96 and 10.22 W m^{-1} K^{-1}, at 25 and 80 wt.% BNNS loading, respectively. Compared to the earlier published data shown in Table 1, the key findings of our work are significantly valuable. The summary of these finding include: (I) the development of dielectric polymer/hBN composites with ultrahigh anisotropic thermoconductivity which is one of the highest levels of anisotropic thermoconductivity in the literature; (II) the enhancement of the through-plane and bulk thermoconductivity of polymer/hBN composites using microcellular foaming which is reported for the first time; (III) in situ exfoliation of hBN platelets using the SCF foaming which is reported for the first time; (IV) using a simple method for manufacturing of dielectric polymer/hBN composites which is readily scalable as compared to complex synthesis procedures mostly used in the literature; and (V) in-depth understanding of the directionally-dependent thermoconductivity of the polymer/hBN composites using direct visualization of the internal microstructure and hBN orientation by X-ray tomography.

Table 1. Thermoconductivity, electrical and dielectric performance of different polymer/boron nitride composites

Materials	Filler content	Thermal conductivity	Dielectric and electrical properties	Fabrication method	Ref.
polydimethylsiloxane / BNNS+ FeCo	50/30 wt%	$K_{//}$=2.25	-	self-assembly and magnetic alignment	59
polyimide/hBN	30 vol%	$K_{//}$=2.81; $K_{\perp}$ = 0.73	-	ball milling, compression and sintering	61
epoxy/BNNS	15 vol%	$K_{//}$=6.07; $K_{//}$/ $K_{\perp}$=12	σ_{dc} =2 × 10^{-12} S/cm	nacre-mimetic 3D filler network	60
PVDF/BNNS	33 wt.%	$K_{//}$=16.3; $K_{//}$/ $K_{\perp}$=21	*tan* δ ~0.05 at 10^2 Hz	electrospinning followed by folding and pressing	47
epoxy/hBN	20 wt.%	K_{total}=0.85	-	surface modification with iron oxide and magnetic alignment	11
PS/BNNS	67.6 vol.%	K_{total}~1.1	ε' ~4.5; *tan* δ ~0.02 at 10^2	reversible fragmentation chain	24

			Hz	transfer polymerization	
PMMA/BNNS	80 wt.%	$K_{\perp}$=10.22	-	exfoliation using superacid and functionalization	19
polytetrafluoroethylene (PTFE)/ hBN+AlN	30 vol.%	$K_{\perp}$=1.04	ε' ~3.4; *tan* δ ~0.04 at 10^2 Hz	solution mixing and hot pressing	27
PMMA/BNNS	56.1 wt. %	K_{total} ~6.75	ε' ~3.1–2.9 *; tan* δ <0.028	carbothermal reduction CVD substitution reaction	4
Aromatic polyimides/hBN	60 vol.%	$K_{//}$=17.5 $K_{\perp}$~2.3	-	hBN-containing slurry, sonication and in-situ polymerization	17
HDPE/hBN solid	23.2 vol%	$K_{//}$=10.1; $K_{//}/K_{\perp}$=36; K_{total}=1.73	ε' ~3 *; tan* δ=0.008; σ_{dc} =6 × 10^{-14} S/cm	melt compounding and injection molding	this work
HDPE/ hBN 20% porosity	15.7 vol%	$K_{//}$=1.55; $K_{//}/K_{\perp}$=1.8; K_{total}=1.45	ε' ~2.8 *; tan* δ=0.007; σ_{dc} =5 × 10^{-14} S/cm	melt compounding, injection molding and physical foaming	this work
HDPE/ hBN 10% porosity	20.9 vol%	$K_{//}$=3.21; $K_{//}/K_{\perp}$=2.3; K_{total}=2.07	ε' ~2.9 *; tan* δ=0.006; σ_{dc} =7 × 10^{-14} S/cm	melt compounding, injection molding and physical foaming	this work

3. Summary & Conclusions

A new class of microstructure-tailored dielectric polymer/hBN composites with isotropic and anisotropic thermoconductivity was developed. The HDPE/hBN composites with tailored structures were developed through a scalable technique of melt compounding followed by injection molding. The directionally-dependent thermal transport properties of the polymer/hBN composites were further understood through X-ray tomography assessment of the internal structure of the composites which revealed an anisotropic structure in the case of the solid composites and an isotropic structure in the case of the porous composites. Due to high shear rate, induced during injection, a high level of hBN platelet orientation was generated within the polymer matrix as revealed by x-ray tomography. This structure resulted in significant anisotropic

thermoconductivity in the solid HDPE/hBN composites. For instance, the in-plane thermoconductivity of the solid HDPE/23.2 vol.% hBN composites reached to 10.1±0.5 $Wm^{-1}K^{-1}$, while the through-plane thermoconductivity was 0.28 $Wm^{-1}K^{-1}$. By the introduction of a small amount of porosity (10%) through physical foaming, (i) shear-induced orientation of hBN was changed into random orientation with increased local and 3D interconnections of hBN; and (ii) dispersion and exfoliation of hBN were further enhanced. This resulted in higher bulk thermoconductivity of the porous HDPE/hBN composites (10% porosity), as compared to their solid counterparts. Both solid and porous HDPE/hBN composites were highly electrically insulating with low ε' (> 3.00±0.04) and ultralow *tan* δ (> 0.0068 at 100 Hz). Therefore, this work presents a simple manufacturing method to produce lightweight electrically insulative dielectric polymer/hBN composites with tailored thermoconductivity for heat dissipation components in high operation speed microelectronic devices.

4. Materials and Methods

4.1. Materials and Sample Preparation

A high-density-polypropylene (HDPE), Marlex® HHM 5502BN with a specific gravity of 0.955 g cm^{-3} and melt flow index of 0.35 dg/min^{-1} (230 ºC/2.16 kg), was selected as the matrix. The HDPE was loaded with PolarTherm™ PT110 hBN, with mean particle size of 45 μm, surface area of 0.6 m^2/g, and specific gravity of 2.1 $g.cm^{-3}$, provided by Mometive™. Commercial nitrogen (N_2, Linde Gas, Canada) was utilized as blowing agent.

A TDS-20 twin-screw extruder (L/D=40; screw diameter =22 mm) was used to produce HDPE/40 wt.% hBN masterbatch by melt mixing. More details on producing the masterbatch are provided in Supporting Information (Section S3).

An injection molding machine (Arburg Allrounder 270/320C,) equipped with MuCell® technology (Trexel, Inc., Woburn, Massachusetts) with 30-mm diameter screw was used to fabricate the solid and porous HDPE/hBN composites. The processing parameters used to produce the solid and porous composites were obtained such as to maintain the integrity of the composites' microstructure. The processing parameters used in this work are summarized in **Table S1**.

The solid HDPE/hBN composites were injection molded without foaming. For the porous composites, the MuCell® module (built-on module of the injection molding machine) was employed to inject 0.4 wt.% N_2 in supercritical form into the barrel. Due to high pressure in the mixing section generated by the screw, gas can be dissolved in the polymer to produce a homogenized polymer/hBN/gas mixture. After SCF treatment, the resulting mixture was injected into a low-pressure environment (mold cavity) where foaming took place and a porous structure was generated. The mold was partially filled with the polymer/hBN/gas mixture to produce polymer/hBN composites with 10% and 20% porosity. More details regarding the injection molding processed HDPE/hBN composites are provided in Supporting Information (Section S3). A schematic representation of the injection molding process and fabricated samples is shown in **Figure S5**.

4.2. Characterization

Wide Angle X-ray Diffraction analyses using Rigaku MiniFlex 600 X-ray diffractometer were performed on the hBN powder, neat HDPE, and solid and porous injection molded composites to investigate the exfoliation/dispersion of hBN platelets in the polymer matrix. The microstructure of composites (arrangement, orientation, exfoliation and dispersion of the hBNplatelets) were investigated using scanning electron microscopy (SEM; Quanta EFG250) and transmission electron microscopy (TEM; FEI Tecnai 20). The internal structure of the HDPE/hBN composites

were characterized using laboratory X-ray tomography. Acquisition was performed with an Easytom laboratory X-ray computed tomography apparatus (RX Solutions, France). X-ray tomography can reach very high resolution as has been reported by Guo et al. [62], thanks to the very small spot size (down to 0.5 μm) provided by a LaB_6 cathode leading to a decrease in the geometrical blur. For the characterization of samples in this study, the polycoromatic X-ray was operated with a LaB cathode at a voltage of 70 kV and intensity of 150 μA. 4000 X-ray projections were collected on a CCD camera with an exposure time of 0.4 seconds to obtain a 3D volume. Acquisition was performed with voxel sizes of 0.7 μm and 1.5 μm at different depths along the sample axis. Continuous rotation was used without averaging. A filtered back projection Feldkamp algorithm was used to reconstruct the data; this was followed by image-processing and visualization with Fiji freeware [63]. X-ray tomography consists of reconstructing a volume image from 360 ° 2D radiographs. It is based on the absorption difference of the constituent phases of the materials and depends on the Beer-Lambert law. For a given path where the X-rays pass through the material, the ratio between the number of photons transmitted N and the number of incident photons N_0 is defined by $\frac{N}{N_0} = \exp\left[-\int \mu(s)\, ds\right]$[39]; where μ(s) is the absorption coefficient of the material along the path *s* which depends on the atomic number Z, the density of the materials crossed and the energy of the incident photons.

The thermal conductivity measurement of hBN/HDPE composites was performed by transient hot disk method according to ISO/DIS 22007-2.2. A transient plane source (TPS) 2500 (Therm Test Inc., Sweden) thermal constants analyzer with a Kapton sensor (5465), was employed to measure the thermoconductivity of the samples under ambient conditions **(Figure S6)**. The Standard Measurement Module was used to measure the bulk/average thermoconductivity of the fabricated samples. The Anisotropic Measurement Module of the TPS 2500 was employed to measure in-

plane and through-plane thermoconductivity of the fabricated composites. This measurement module requires the specific heat capacity of the samples which can be accurately measured with a the dedicated TPS measurement module.

Optimized combinations of the measurement time and the heating power were selected for the fabricated composites based on their heat transport properties. The transient plane source theory assumes that the sensor is located in an infinite medium of sample and, therefore, the heat penetration should not exceed the boundaries of the samples. **Figure S7** shows the heat penetration (probing depth) during thermal conductivity measurement using the Anisotropic Measurement Module. As shown in Figure S7, the proper combinations of the power output and the measurement time were selected so that the penetration of heat does not exceed the boundaries of the samples. It is also notable that the heat is dissipated more significantly in-plane in the solid samples as compared to porous counterparts which is the indication of their anisotropic thermal conductivity. By increasing the porosity from 10% to 20% the heat dissipation through-plane and in-plane becomes more uniform which can be related to the higher level of isotropic thermoconductivity in porous samples. The later result is found in a good agreement with the smaller $K_{//}/K_{\perp}$ ratio for porous samples as compared with solid composites.

More details on thermal conductivity measurement using the TPS method is presented in Supporting Information (Section S4), including Figures S6 and S7. For a theoretical standpoint, the interested readers are referred to research works presented by Gustafsson [64], Gustavsson et al. [65], Miller et al. [66] and He [67].

The electrical conductivity, ε' and $tan\ \delta$ of the hBN/HDPE composites were analyzed over a wide frequency range (1 Hz to $1\times10^{+5}$ Hz) using an Alpha-A dielectric impedance analyzer (Novocontrol Technologies).

5. Associated content

Supporting Information:

The processing parameters and method of sample preparation, the schematic representation of the injection molding process and fabricated samples, schematic illustration of ISO/DIS 22007-2.2 along with details for measuring the thermal conductivity and SEM images of composites.

6. Acknowledgment

The authors gratefully acknowledge financial support from NanoXplore Inc. and the Natural Sciences and Engineering Research Council of Canada (NSERC).

References

(1) Cho, J.; Goodson, K. E. Thermal Transport: Cool Electronics. *Nat. Mater.* **2015**, *14* (2), 136–137. https://doi.org/10.1038/nmat4194.

(2) Liang, Q.; Yao, X.; Wang, W.; Liu, Y.; Wong, C. P. A Three-Dimensional Vertically Aligned Functionalized Multilayer Graphene Architecture: An Approach for Graphene-Based Thermal Interfacial Materials. *ACS Nano* **2011**, *5* (3), 2392–2401. https://doi.org/10.1021/nn200181e.

(3) Hamidinejad, M.; Chu, R.; Zhao, B.; Park, C. B.; Filleter, T. Enhanced Thermal Conductivity of Graphene Nanoplatelet-Polymer Nanocomposites Fabricated via Supercritical Fluid Assisted In-Situ Exfoliation. *ACS Appl. Mater. Interfaces* **2018**, *10* (1), 1225−1236. https://doi.org/10.1021/acsami.7b15170.

(4) Xue, Y.; Zhou, X.; Zhan, T.; Jiang, B.; Guo, Q.; Fu, X.; Shimamura, K.; Xu, Y.; Mori, T.; Dai, P.; et al. Densely Interconnected Porous BN Frameworks for Multifunctional and Isotropically Thermoconductive Polymer Composites. *Adv. Funct. Mater.* **2018**, *28* (29), 1801205. https://doi.org/10.1002/adfm.201801205.

(5) Miller, R. D. In Search of Low-k Dielectrics. *Science (80-.).* **1999**, *286* (5439), 421–423. https://doi.org/10.1126/science.286.5439.421.

(6) Huang, X.; Zhi, C.; Jiang, P.; Golberg, D.; Bando, Y.; Tanaka, T. Polyhedral Oligosilsesquioxane-Modified Boron Nitride Nanotube Based Epoxy Nanocomposites: An Ideal Dielectric Material with High Thermal Conductivity. *Adv. Funct. Mater.* **2013**, *23* (14), 1824–1831. https://doi.org/10.1002/adfm.201201824.

(7) Huang, X.; Jiang, P.; Tanaka, T. A Review of Dielectric Polymer Composites with High Thermal Conductivity. *IEEE Electr. Insul. Mag.* **2011**, *27* (4), 8–16. https://doi.org/10.1109/MEI.2011.5954064.

(8) Zhou, T.; Wang, X.; Gu, M.; Xiong, D. Study on Mechanical, Thermal and Electrical Characterizations of Nano-SiC/Epoxy Composites. *Polym. J.* **2009**, *41* (1), 51–57. https://doi.org/10.1295/polymj.PJ2008173.

(9) Song, W. L.; Wang, P.; Cao, L.; Anderson, A.; Meziani, M. J.; Farr, A. J.; Sun, Y. P. Polymer/Boron Nitride Nanocomposite Materials for Superior Thermal Transport Performance. *Angew. Chemie - Int. Ed.* **2012**, *51* (26), 6498–6501. https://doi.org/10.1002/anie.201201689.

(10) Yuan, C.; Duan, B.; Li, L.; Xie, B.; Huang, M.; Luo, X. Thermal Conductivity of Polymer-Based

Composites with Magnetic Aligned Hexagonal Boron Nitride Platelets. *ACS Appl. Mater. Interfaces* **2015**, *7* (23), 13000–13006. https://doi.org/10.1021/acsami.5b03007.

(11) Lin, Z.; Liu, Y.; Raghavan, S.; Moon, K. S.; Sitaraman, S. K.; Wong, C. P. Magnetic Alignment of Hexagonal Boron Nitride Platelets in Polymer Matrix: Toward High Performance Anisotropic Polymer Composites for Electronic Encapsulation. *ACS Appl. Mater. Interfaces* **2013**, *5* (15), 7633–7640. https://doi.org/10.1021/am401939z.

(12) Xu, Y.; Chung, D. D. L. Increasing the Thermal Conductivity of Boron Nitride and Aluminum Nitride Particle Epoxy-Matrix Composites by Particle Surface Treatments. *Compos. Interfaces* **2000**, *7* (4), 243–256. https://doi.org/10.1163/156855400750244969.

(13) Wang, Z.; Cheng, Y.; Yang, M.; Huang, J.; Cao, D.; Chen, S.; Xie, Q.; Lou, W.; Wu, H. Dielectric Properties and Thermal Conductivity of Epoxy Composites Using Core/Shell Structured Si/SiO2/Polydopamine. *Compos. Part B Eng.* **2018**, *140*, 83–90. https://doi.org/10.1016/j.compositesb.2017.12.004.

(14) Cassabois, G.; Valvin, P.; Gil, B. Hexagonal Boron Nitride Is an Indirect Bandgap Semiconductor. *Nat. Photonics* **2016**, *10* (4), 262–266. https://doi.org/10.1038/nphoton.2015.277.

(15) Watanabe, K.; Taniguchi, T.; Kanda, H. Direct-Bandgap Properties and Evidence for Ultraviolet Lasing of Hexagonal Boron Nitride Single Crystal. *Nat. Mater.* **2004**, *3* (6), 404–409. https://doi.org/10.1038/nmat1134.

(16) Laturia, A.; Van de Put, M. L.; Vandenberghe, W. G. Dielectric Properties of Hexagonal Boron Nitride and Transition Metal Dichalcogenides: From Monolayer to Bulk. *npj 2D Mater. Appl.* **2018**, *2* (1), 6. https://doi.org/10.1038/s41699-018-0050-x.

(17) Tanimoto, M.; Yamagata, T.; Miyata, K.; Ando, S. Anisotropic Thermal Diffusivity of Hexagonal Boron Nitride-Filled Polyimide Films: Effects of Filler Particle Size, Aggregation, Orientation, and Polymer Chain Rigidity. *ACS Appl. Mater. Interfaces* **2013**, *5* (10), 4374–4382. https://doi.org/10.1021/am400615z.

(18) Balandin, A. A. Thermal Properties of Graphene and Nanostructured Carbon Materials. *Nat. Mater.* **2011**, *10* (8), 569–581. https://doi.org/10.1038/nmat3064.

(19) Morishita, T.; Okamoto, H. Facile Exfoliation and Noncovalent Superacid Functionalization of Boron Nitride Nanosheets and Their Use for Highly Thermally Conductive and Electrically Insulating Polymer Nanocomposites. *ACS Appl. Mater. Interfaces* **2016**, *8* (40), 27064–27073. https://doi.org/10.1021/acsami.6b08404.

(20) Lin, Z.; Mcnamara, A.; Liu, Y.; Moon, K. sik; Wong, C. P. Exfoliated Hexagonal Boron Nitride-Based Polymer Nanocomposite with Enhanced Thermal Conductivity for Electronic Encapsulation. *Compos. Sci. Technol.* **2014**, *90*, 123–128. https://doi.org/10.1016/j.compscitech.2013.10.018.

(21) Yu, C.; Zhang, J.; Tian, W.; Fan, X.; Yao, Y. Polymer Composites Based on Hexagonal Boron Nitride and Their Application in Thermally Conductive Composites. *RSC Adv.* **2018**, *8* (39), 21948–21967. https://doi.org/10.1039/c8ra02685h.

(22) Su, Z.; Wang, H.; He, J.; Guo, Y.; Qu, Q.; Tian, X. Fabrication of Thermal Conductivity Enhanced Polymer Composites by Constructing an Oriented Three-Dimensional Staggered Interconnected Network of Boron Nitride Platelets and Carbon Nanotubes. *ACS Appl. Mater. Interfaces* **2018**, *10*, acsami.8b09703. https://doi.org/10.1021/acsami.8b09703.

(23) Guo, Y.; Leung, S. N. Thermally Conductive Polybutylene Terephthalate/Hexagonal Boron Nitride Composites with Bimodal Filler Size Distribution. *Mater. Chem. Phys.* **2018**, *214*, 221–228. https://doi.org/10.1016/j.matchemphys.2018.04.073.

(24) Huang, X.; Wang, S.; Zhu, M.; Yang, K.; Jiang, P.; Bando, Y.; Golberg, D.; Zhi, C. Thermally Conductive, Electrically Insulating and Melt-Processable Polystyrene/Boron Nitride Nanocomposites Prepared by in Situ Reversible Addition Fragmentation Chain Transfer Polymerization. *Nanotechnology* **2015**, *26* (1), 015705. https://doi.org/10.1088/0957-4484/26/1/015705.

(25) Cui, Z.; Martinez, A. P.; Adamson, D. H. PMMA Functionalized Boron Nitride Sheets as Nanofillers. *Nanoscale* **2015**, *7* (22), 10193–10197. https://doi.org/10.1039/c5nr00936g.

(26) Yang, N.; Zeng, X.; Lu, J.; Sun, R.; Wong, C. Effect of Chemical Functionalization on the Thermal

Conductivity of 2D Hexagonal Boron Nitride. *Appl. Phys. Lett.* **2018**, *113* (17), 1–11. https://doi.org/10.1063/1.5050293.

(27) Pan, C.; Kou, K.; Zhang, Y.; Li, Z.; Wu, G. Enhanced Through-Plane Thermal Conductivity of PTFE Composites with Hybrid Fillers of Hexagonal Boron Nitride Platelets and Aluminum Nitride Particles. *Compos. Part B Eng.* **2018**, *153*, 1–8. https://doi.org/10.1016/j.compositesb.2018.07.019.

(28) Su, Z.; Wang, H.; Ye, X.; Tian, K.; Huang, W.; He, J.; Guo, Y.; Tian, X. Synergistic Enhancement of Anisotropic Thermal Transport Flexible Polymer Composites Filled with Multi-Layer Graphene (MG) and Mussel-Inspiring Modified Hexagonal Boron Nitride (h-BN). *Compos. Part A Appl. Sci. Manuf.* **2018**, *111*, 12–22. https://doi.org/10.1016/j.compositesa.2018.04.021.

(29) Zhao, B.; Hamidinejad, M.; Zhao, C.; Li, R.; Wang, S.; Kazemi, Y.; Park, C. B. A Versatile Foaming Platform to Fabricate Polymer/Carbon Composites with High Dielectric Permittivity and Ultra-Low Dielectric Loss. *J. Mater. Chem. A* **2019**, *7* (1), 133–140. https://doi.org/10.1039/C8TA05556D.

(30) Hamidinejad, M.; Zhao, B.; Zandieh, A.; Moghimian, N.; Filleter, T.; Park, C. B. Enhanced Electrical and Electromagnetic Interference Shielding Properties of Polymer-Graphene Nanoplatelet Composites Fabricated via Supercritical-Fluid Treatment and Physical Foaming. *ACS Appl. Mater. Interfaces* **2018**, *10* (36), 30752−30761. https://doi.org/10.1021/acsami.8b10745.

(31) Hamidinejad, M.; Zhao, B.; Chu, R. K. M.; Moghimian, N.; Naguib, H. E.; Filleter, T.; Park, C. B. Ultralight Microcellular Polymer-Graphene Nanoplatelet Foams with Enhanced Dielectric Performance. *ACS Appl. Mater. Interfaces* **2018**, *10* (23), 19987–19998. https://doi.org/10.1021/acsami.8b03777.

(32) Nguyen, Q. T.; Baird, D. G. An Improved Technique for Exfoliating and Dispersing Nanoclay Particles into Polymer Matrices Using Supercritical Carbon Dioxide. *Polymer (Guildf).* **2007**, *48* (23), 6923–6933. https://doi.org/10.1016/j.polymer.2007.09.015.

(33) Ling, J.; Zhai, W.; Feng, W.; Shen, B.; Zhang, J.; Zheng, W. G. Facile Preparation of Lightweight Microcellular Polyetherimide/Graphene Composite Foams for Electromagnetic Interference Shielding. *ACS Appl. Mater. Interfaces* **2013**, *5* (7), 2677–2684. https://doi.org/10.1021/am303289m.

(34) Shen, B.; Li, Y.; Zhai, W.; Zheng, W. Compressible Graphene-Coated Polymer Foams with Ultralow Density for Adjustable Electromagnetic Interference (EMI) Shielding. *ACS Appl. Mater. Interfaces* **2016**, *8* (12), 8050–8057. https://doi.org/10.1021/acsami.5b11715.

(35) Okamoto, M.; Nam, P. H.; Maiti, P.; Kotaka, T.; Nakayama, T.; Takada, M.; Ohshima, M.; Usuki, A.; Hasegawa, N.; Okamoto, H. Biaxial Flow-Induced Alignment of Silicate Layers in Polypropylene/Clay Nanocomposite Foam. *Nano Lett.* **2001**, *1* (9), 503–505. https://doi.org/10.1021/nl010051+.

(36) Zhao, H.; Zhao, G.; Turng, L.-S.; Peng, X. Enhancing Nanofiller Dispersion Through Prefoaming and Its Effect on the Microstructure of Microcellular Injection Molded Polylactic Acid/Clay Nanocomposites. *Ind. Eng. Chem. Res.* **2015**, *54* (28), 7122–7130. https://doi.org/10.1021/acs.iecr.5b01130.

(37) Ellingham, T.; Duddleston, L.; Turng, L. S. Sub-Critical Gas-Assisted Processing Using CO2 Foaming to Enhance the Exfoliation of Graphene in Polypropylene + Graphene Nanocomposites. *Polym. (United Kingdom)* **2017**, *117*, 132–139. https://doi.org/10.1016/j.polymer.2017.04.028.

(38) Maire, E.; Colombo, P.; Adrien, J.; Babout, L.; Biasetto, L. Characterization of the Morphology of Cellular Ceramics by 3D Image Processing of X-Ray Tomography. *J. Eur. Ceram. Soc.* **2007**, *27* (4), 1973–1981. https://doi.org/10.1016/j.jeurceramsoc.2006.05.097.

(39) Baruchel, J.; Buffière, J. Y.; Maire, E.; Merle, P.; Peix, G. *X-Ray Tomography in Material Science*; Hermès Science Publications, 2000.

(40) Motlagh, G. H.; Hrymak, A. N.; Thompson, M. R. Improved Through-Plane Electrical Conductivity in a Carbon-Filled Thermoplastic via Foaming. *Polym. Eng. Sci.* **2008**, *48* (4), 687–696. https://doi.org/10.1002/pen.21001.

(41) Wong, A.; Wijnands, S. F. L.; Kuboki, T.; Park, C. B. Mechanisms of Nanoclay-Enhanced Plastic Foaming Processes: Effects of Nanoclay Intercalation and Exfoliation. *J. Nanoparticle Res.* **2013**,

15 (8), 1815–15. https://doi.org/10.1007/s11051-013-1815-y.
(42) Zhang, B.; Wu, Q.; Yu, H.; Bulin, C.; Sun, H.; Li, R.; Ge, X.; Xing, R. High-Efficient Liquid Exfoliation of Boron Nitride Nanosheets Using Aqueous Solution of Alkanolamine. *Nanoscale Res. Lett.* **2017**, *12* (1). https://doi.org/10.1186/s11671-017-2366-4.
(43) Deepika, A.; Li, L. H.; Glushenkov, A. M.; Hait, S. K.; Hodgson, P.; Chen, Y. High-Efficient Production of Boron Nitride Nanosheets via an Optimized Ball Milling Process for Lubrication in Oil. *Sci. Rep.* **2014**, *4* (1), 7288. https://doi.org/10.1038/srep07288.
(44) Xue, Y.; Liu, Q.; He, G.; Xu, K.; Jiang, L.; Hu, X.; Hu, J. *Excellent Electrical Conductivity of the Exfoliated and Fluorinated Hexagonal Boron Nitride Nanosheets*; 2013; Vol. 8. https://doi.org/10.1186/1556-276X-8-49.
(45) Wakabayashi, K.; Pierre, C.; Diking, D. A.; Ruoff, R. S.; Ramanathan, T.; Catherine Brinson, L.; Torkelson, J. M. Polymer - Graphite Nanocomposites: Effective Dispersion and Major Property Enhancement via Solid-State Shear Pulverization. *Macromolecules* **2008**, *41* (6), 1905–1908. https://doi.org/10.1021/ma071687b.
(46) Pu, N. W.; Wang, C. A.; Sung, Y.; Liu, Y. M.; Ger, M. Der. Production of Few-Layer Graphene by Supercritical CO2 Exfoliation of Graphite. *Mater. Lett.* **2009**, *63* (23), 1987–1989. https://doi.org/10.1016/j.matlet.2009.06.031.
(47) Chen, J.; Huang, X.; Sun, B.; Jiang, P. Highly Thermally Conductive Yet Electrically Insulating Polymer/Boron Nitride Nanosheets Nanocomposite Films for Improved Thermal Management Capability. *ACS Nano* **2019**, *13* (1), 337–345. https://doi.org/10.1021/acsnano.8b06290.
(48) Shtein, M.; Nadiv, R.; Buzaglo, M.; Kahil, K.; Regev, O. Thermally Conductive Graphene-Polymer Composites: Size, Percolation, and Synergy Effects. *Chem. Mater.* **2015**, *27* (6), 2100–2106. https://doi.org/10.1021/cm504550e.
(49) Yuan, J.; Yao, S.; Poulin, P. Dielectric Constant of Polymer Composites and the Routes to High-k or Low-k Nanocomposite Materials. In *Polymer Nanocomposites: Electrical and Thermal Properties*; Springer International Publishing: Cham, 2016; pp 3–28. https://doi.org/10.1007/978-3-319-28238-1_1.
(50) Yang, K.; Huang, X.; Huang, Y.; Xie, L.; Jiang, P. Fluoro-Polymer@BaTiO3 Hybrid Nanoparticles Prepared via RAFT Polymerization: Toward Ferroelectric Polymer Nanocomposites with High Dielectric Constant and Low Dielectric Loss for Energy Storage Application. *Chem. Mater.* **2013**, *25* (11), 2327–2338. https://doi.org/10.1021/cm4010486.
(51) Ameli, A.; Nofar, M.; Park, C. B.; Pötschke, P.; Rizvi, G. Polypropylene/Carbon Nanotube Nano/ Microcellular Structures with High Dielectric Permittivity, Low Dielectric Loss, and Low Percolation Threshold. *Carbon N. Y.* **2014**, *71*, 206–217. https://doi.org/10.1016/j.carbon.2014.01.031.
(52) Lin, S.; Ye, F.; Ma, J.; Ding, J.; Liu, Q.; Dong, S. Fabrication and Properties of Porous Boron Nitride/Silicon Oxynitride Ceramic Composites via Gas Pressure Sintering. *Mater. Des.* **2015**, *87*, 272–277. https://doi.org/10.1016/j.matdes.2015.08.032.
(53) Xue, Y.; Dai, P.; Zhou, M.; Wang, X.; Pakdel, A.; Zhang, C.; Weng, Q.; Takei, T.; Fu, X.; Popov, Z. I.; et al. Multifunctional Superelastic Foam-Like Boron Nitride Nanotubular Cellular-Network Architectures. *ACS Nano* **2017**, *11* (1), 558–568. https://doi.org/10.1021/acsnano.6b06601.
(54) Purushothaman, R. Amine Functionalized SBA-15/Terpolyimide Composites with Low Dielectric Constant. *J. Porous Mater.* **2015**, *22* (3), 585–594. https://doi.org/10.1007/s10934-015-9930-z.
(55) Vo, L. T.; Anastasiadis, S. H.; Giannelis, E. P. Dielectric Study of Poly(Styrene-Co-Butadiene) Composites with Carbon Black, Silica, and Nanoclay. *Macromolecules* **2011**, *44* (15), 6162–6171. https://doi.org/10.1021/ma200044c.
(56) Wang, B.; Liang, G.; Jiao, Y.; Gu, A.; Liu, L.; Yuan, L.; Zhang, W. Two-Layer Materials of Polyethylene and a Carbon Nanotube/Cyanate Ester Composite with High Dielectric Constant and Extremely Low Dielectric Loss. *Carbon N. Y.* **2013**, *54*, 224–233. https://doi.org/10.1016/j.carbon.2012.11.033.
(57) Antunes, M.; Mudarra, M.; Velasco, J. I. Broad-Band Electrical Conductivity of Carbon Nanofibre-Reinforced Polypropylene Foams. *Carbon N. Y.* **2011**, *49* (2), 708–717.

https://doi.org/10.1016/j.carbon.2010.10.032.
(58) Jin, Y.; Xia, N.; Gerhardt, R. A. Enhanced Dielectric Properties of Polymer Matrix Composites with BaTiO3 and MWCNT Hybrid Fillers Using Simple Phase Separation. *Nano Energy* **2016**, *30*, 407–416. https://doi.org/10.1016/j.nanoen.2016.10.033.
(59) Yuan, J.; Qian, X.; Meng, Z.; Yang, B.; Liu, Z. Q. Highly Thermally Conducting Polymer-Based Films with Magnetic Field-Assisted Vertically Aligned Hexagonal Boron Nitride for Flexible Electronic Encapsulation. *ACS Appl. Mater. Interfaces* **2019**, *11* (19), 17915–17924. https://doi.org/10.1021/acsami.9b06062.
(60) Han, J.; Du, G.; Gao, W.; Bai, H. An Anisotropically High Thermal Conductive Boron Nitride/Epoxy Composite Based on Nacre-Mimetic 3D Network. *Adv. Funct. Mater.* **2019**, *29* (13), 1–9. https://doi.org/10.1002/adfm.201900412.
(61) Wang, H.; Ding, D.; Liu, Q.; Chen, Y.; Zhang, Q. Highly Anisotropic Thermally Conductive Polyimide Composites via the Alignment of Boron Nitride Platelets. *Compos. Part B Eng.* **2019**, *158*, 311–318. https://doi.org/10.1016/j.compositesb.2018.09.104.
(62) Guo, A.; Roso, M.; Modesti, M.; Maire, E.; Adrien, J.; Colombo, P. Characterization of Porosity, Structure, and Mechanical Properties of Electrospun SiOC Fiber Mats. *J. Mater. Sci.* **2015**, *50* (12), 4221–4231. https://doi.org/10.1007/s10853-015-8973-5.
(63) Schindelin, J.; Arganda-Carreras, I.; Frise, E.; Kaynig, V.; Longair, M.; Pietzsch, T.; Preibisch, S.; Rueden, C.; Saalfeld, S.; Schmid, B.; et al. Fiji: An Open-Source Platform for Biological-Image Analysis. *Nat. Methods* **2012**, *9* (7), 676–682. https://doi.org/10.1038/nmeth.2019.
(64) Gustafsson, S. E. Transient Plane Source Techniques for Thermal Conductivity and Thermal Diffusivity Measurements of Solid Materials. *Rev. Sci. Instrum.* **1991**, *62* (3), 797–804. https://doi.org/10.1063/1.1142087.
(65) Gustavsson, M.; Karawacki, E.; Gustafsson, S. E. Thermal Conductivity, Thermal Diffusivity, and Specific Heat of Thin Samples from Transient Measurements with Hot Disk Sensors. *Rev. Sci. Instrum.* **1994**, *65* (12), 3856–3859. https://doi.org/10.1063/1.1145178.
(66) Miller, M. G.; Keith, J. M.; King, J. A.; Edwards, B. J.; Klinkenberg, N.; Schiraldi, D. A. Measuring Thermal Conductivities of Anisotropic Synthetic Graphite-Liquid Crystal Polymer Composites. *Polym. Compos.* **2006**, *27* (4), 388–394. https://doi.org/10.1002/pc.20231.
(67) He, Y. Rapid Thermal Conductivity Measurement with a Hot Disk Sensor: Part 1. Theoretical Considerations. *Thermochim. Acta* **2005**, *436* (1–2), 122–129. https://doi.org/10.1016/j.tca.2005.06.026.

Table of Contents

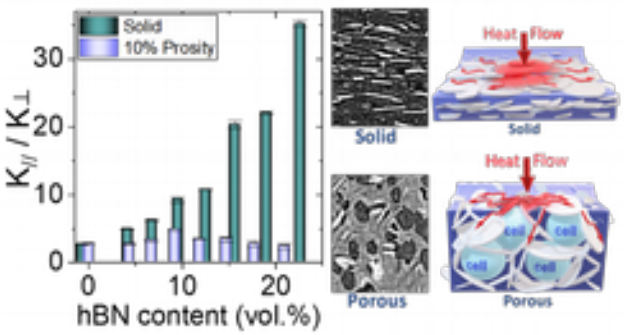

Supporting Information

Insight into the Directional Thermal Transport of Hexagonal Boron Nitride Composites

Mahdi Hamidinejad [a], Azadeh Zandieh [a], Jung H. Lee [a], Justine Papillon [b], Biao Zhao [a], Nima Moghimian [c], Eric Maire [b], Tobin Filleter [a], and Chul B. Park [a]**

[a] Department of Mechanical and Industrial Engineering, University of Toronto, 5 King's College Road, Toronto, Canada M5S 3G8

[b] University of Lyon, INSA de Lyon, MATEIS UMR CNRS 5510, Bât. Saint Exupery, 23 Av. Jean Capelle, F-69621 Villeurbanne, France

[c] NanoXplore Inc., 25 Boul. Montpellier, Saint-Laurent, QC, H4N 2G3

[*]*Corresponding Authors' Information: E-mail:* ***filleter@mie.utoronto.ca; park@mie.utoronto.ca***
Address: 5 King's College Road, Toronto, Ontario M5S 3G8, Canada

- **Cellular microstructure**

Figure S1 shows that cells are smaller in the skin regions of the porous composites and they gradually become larger in the core region. This can be attributed to higher melt strength due to the lower melt temperature in the skin region, where cellular growth is suppressed. **Figure S2** shows the SEM images of HDPE/10.2 vol% hBN and HDPE/19.7 vol% hBN composites.

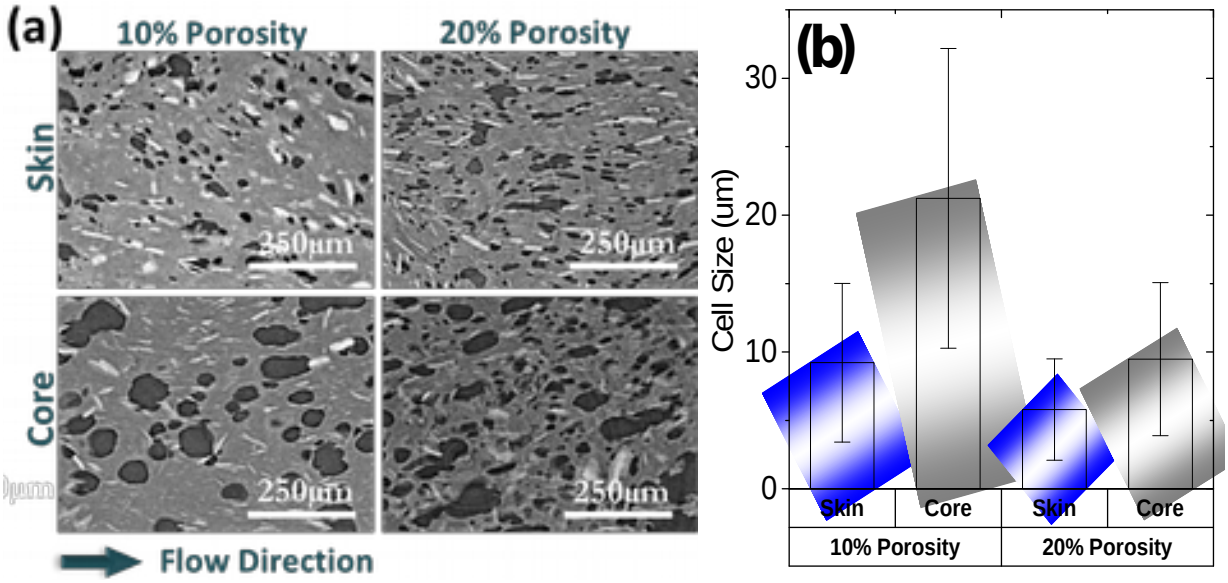

Figure S1. (a) X-ray tomography (top view) of the skin and core regions of the porous HDPE/10.2 vol% hBN composites; (b) the cell sizes of porous HDPE/10.2 vol% hBN composites in the skin and core regions

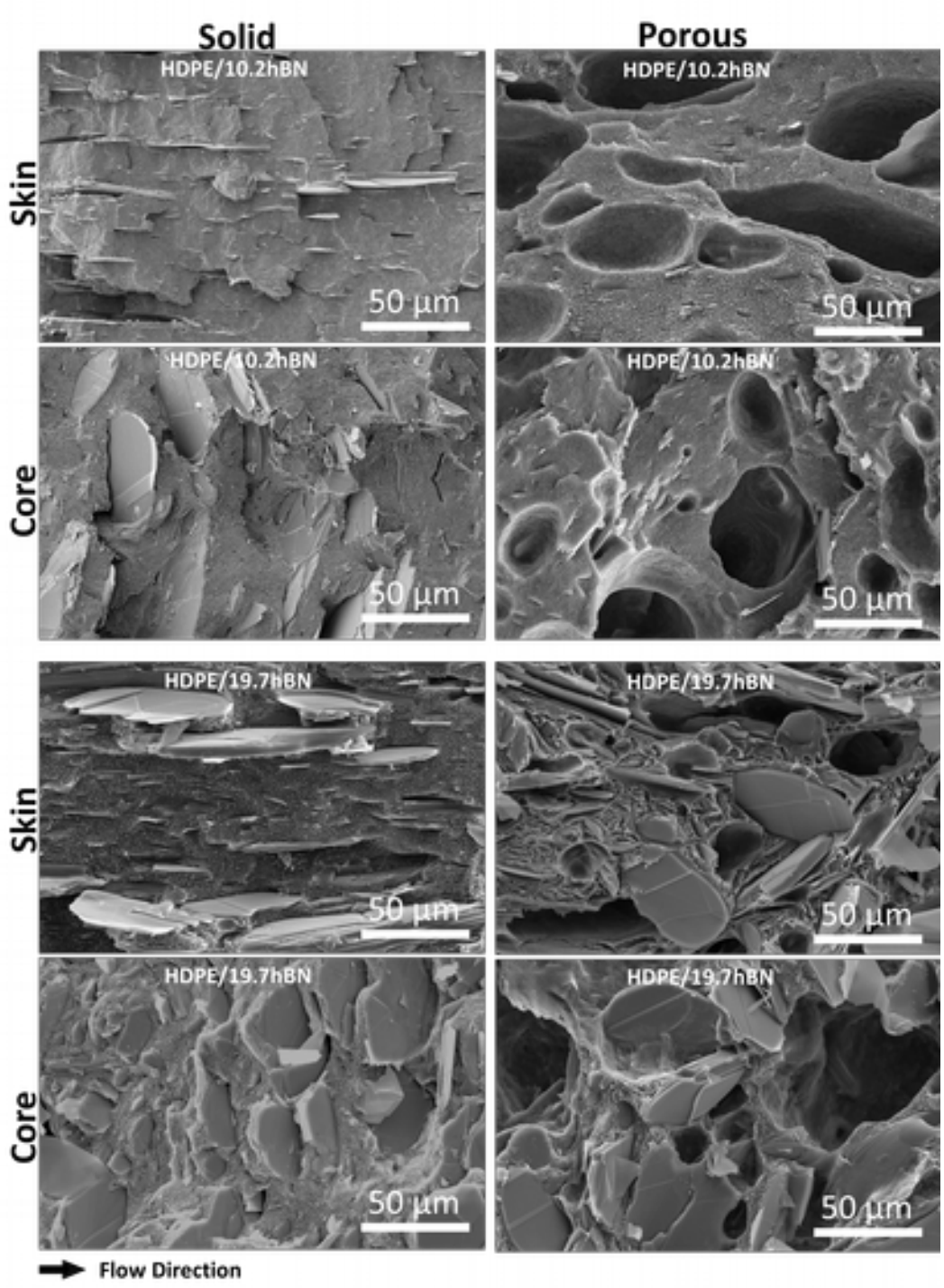

Figure S2. SEM micrographs of the skin and core regions for the solid and porous (with 10% porosity) HDPE/10.2 vol% hBN and HDPE/19.7 vol% hBN composites.

- **Thermal conductivity**

The thermal conductivity variations as a function of the filler content for two different porosities (i.e. 10% and 20%) are presented in **Figure S3**. As shown in Figure S3, the generation of a microcellular structure increased the through-plane thermoconductivity of the solid HDPE/hBN composites up to 478.5%, while their in-plane conductivity decreased by maximum 68.2%.

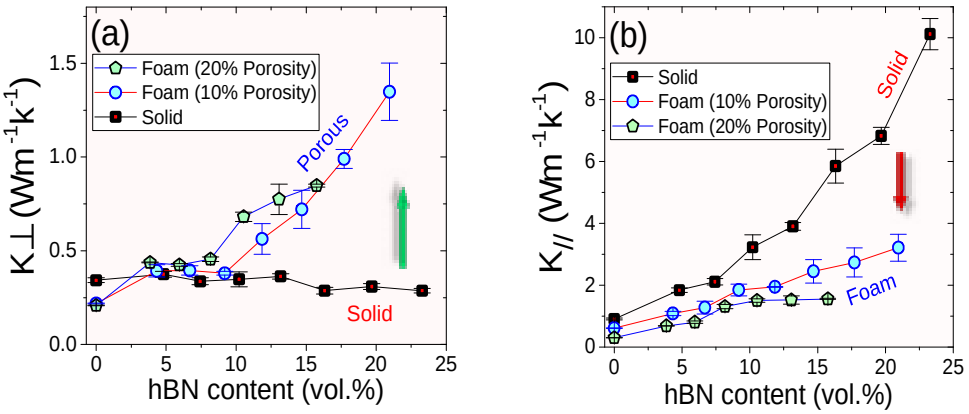

Figure S3. (a) The through-plane thermal conductivity ($K_{\perp}$) and; (b) the in-plane thermal conductivity ($K_{//}$) of solid and porous (10% and 20% porosity) HDPE/hBN composites as a function of the hBN content.

Figure S4 shows the Differential Scanning Calorimetry (DSC) data on the HDPE/hBN composites.

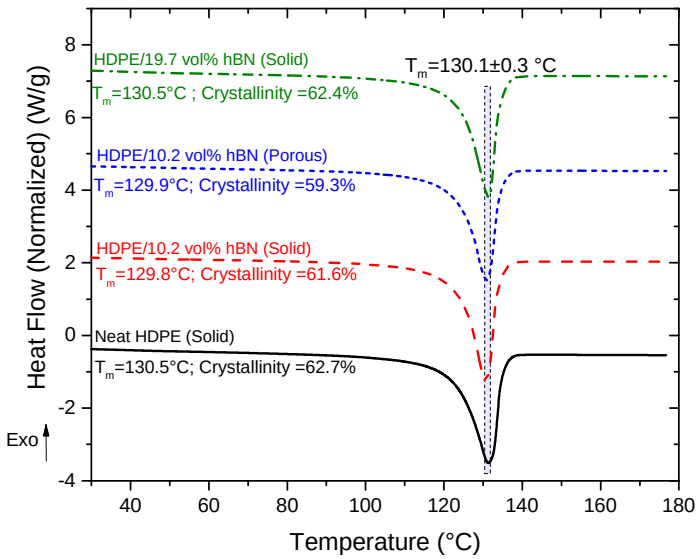

Figure S4. (a) Differential Scanning Calorimetry (DSC) data of the HDPE/hBN composites

- **Sample preparation**

A TDS-20 twin-screw extruder (screw diameter =22 mm; L/D=40) was used to produce HDPE/40 wt.% hBN masterbatch by melt mixing. The temperature profile was set to 180-220°C with a rotational speed of 45 rpm and a throughput of 5 $kg.h^{-1}$. The HDPE/hBN composites with various hBN concentrations were then produced by diluting the HDPE/40 wt.% hBN masterbatch with neat HDPE by mixing in a twin-screw extruder (with diameter of 27 mm and L/D: 40).

An injection molding machine (Arburg Allrounder 270/320C,) equipped with MuCell® technology (Trexel, Inc., Woburn, Massachusetts) with 30-mm diameter screw was used to fabricate the solid and porous HDPE/hBN composites. The mold cavity dimensions were 132 × 108 × 3 mm. More detailed information about the mold used in this research was reported by Lee et al. [1]. Two different types of HDPE/hBN composite, solid injection molded (Solid) and foam injection molded (Porous), were fabricated. The porosity in the porous samples was controlled by partially filling the mold.

The solid HDPE-hBN composites were fabricated using regular injection molding process without SCF-treatment (using N_2 as the SCF) and physical foaming. For the porous composites, the MuCell module was used to inject 0.4 wt.% N_2 at its supercritical state in the barrel. After treating the HDPE-hBN with the SCF, the mold cavity was partially filled with the polymer/hBN/ N_2 mixture. The porosity of the samples is controlled by partial-filling of the mold volume. The utilized processing parameters in this work are summarized in **Table S1**. The conventional and foam injection molding processes are schematically presented in **Figure S5**.

Table S1. Processing parameters used in injection molding of solid and porous composites

	Solid	**Porous**
Melt temperature (°C)	210	210
Barrel pressure (MPa)	16	16
Screw speed (rpm)	300	300
Metering time (s)	12	12
Injection flow rate (cm^3s^{-1})	90	90
Mold temperature (°C)	75	75
Pack/hold pressure (MPa)	30	N/A[a]
Pack/hold time (s)	15	N/A
Cooling time (s)	60	60
Gas injection pressure (MPa)	N/A	24
N_2 content (wt.%)	N/A	0.4
Degree of foaming (porosity) (%)	N/A	10, 20

[a] Not Applicable

The disk-shape solid and porous HDPE/hBN composites were cut from the injection-molded parts at a distance of 100 mm from the cavity gate as shown in **Figure S5**. The samples with a 20 mm diameter × 3 mm thickness were used to measure the thermal conductivity, the dielectric constant, and dielectric loss.

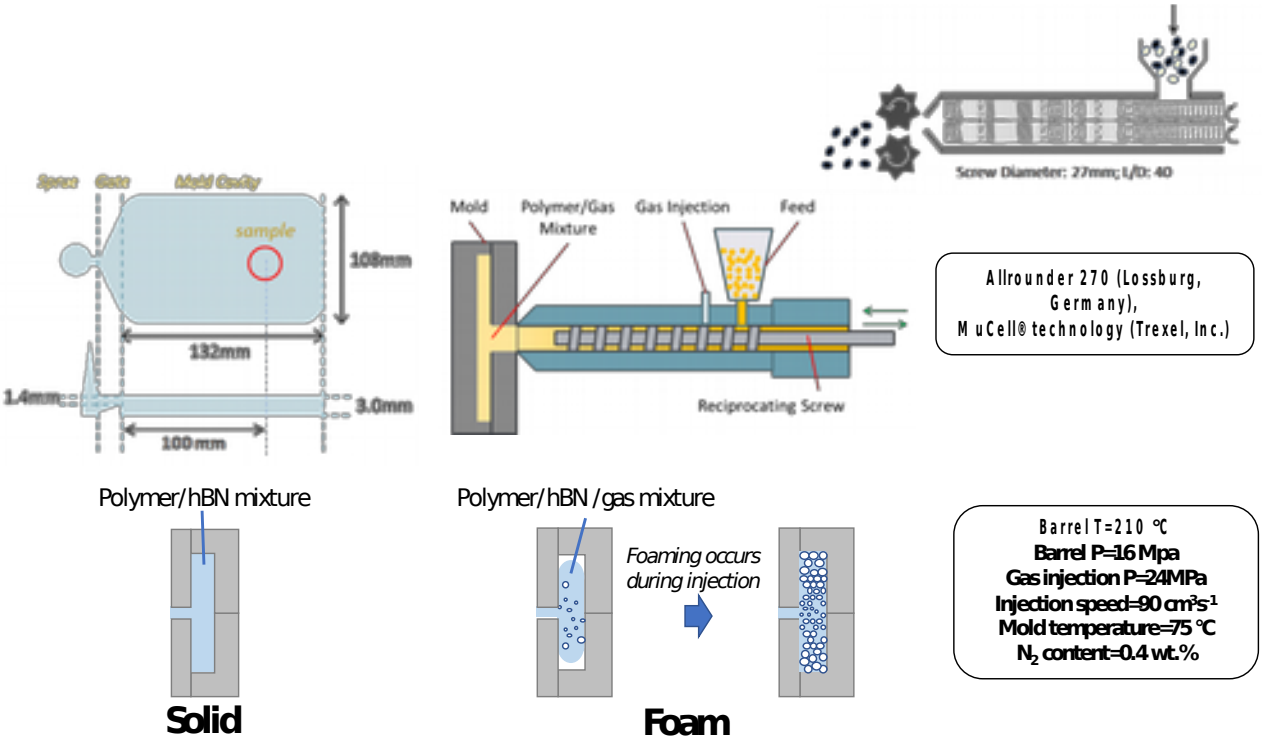

Figure S5. The schematic of regular and foam injection molding processes, the injection molded parts and the location of cut samples.

- **Thermal conductivity measurement**

The thermal conductivity of the HDPE-hBN composites was measured using the transient hot disk method. Measurements were conducted based on the ISO/DIS 22007-2.2 standard. In this technique, an electrically conductive double spiral disk-shape nickel foil sensor acts as a heater to increase the samples' temperature (**Figure S6**). The sensor also works as a dynamic thermometer which records temperature change in the sample as a function of time. The measurement requires two identical pieces of samples and the sensor is placed between two samples (Figure S6). The generated heat pulse dissipates into the samples at a rate which depends on the thermal transport properties of the samples. By recording the temperature with respect to the time response in the sensor, the thermal conductivity can be calculated. For a theoretical standpoint, the interested readers are referred to research works presented by Gustafsson [R2], Gustavsson et al. [R3], Miller et al. [R4] and He [R5].

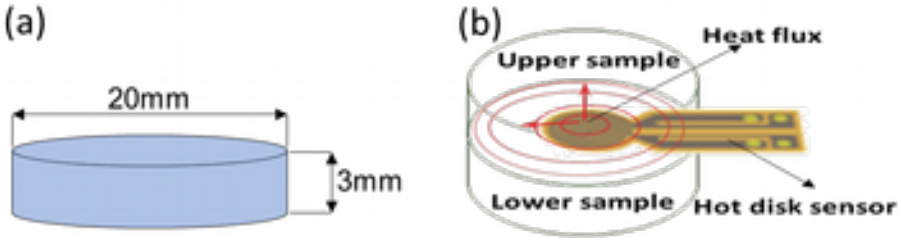

Figure S6. (a) Samples' dimensions; (b) the schematic of the ISO/DIS 22007-2.2 setup for measuring the thermal conductivity using TPS 2500

Based on the ISO/DIS 22007-2.2 standard, Gustafsson [R2], Gustavsson et al. [R3], Miller et al. [R4] and He [R5], the transient plane source method (TPS) is suitable for measuring the thermal conductivity of both isotropic and anisotropic materials. Figure S7 shows the heat penetration (probing depth) during thermal conductivity measurement using Anisotropic Measurement Module.

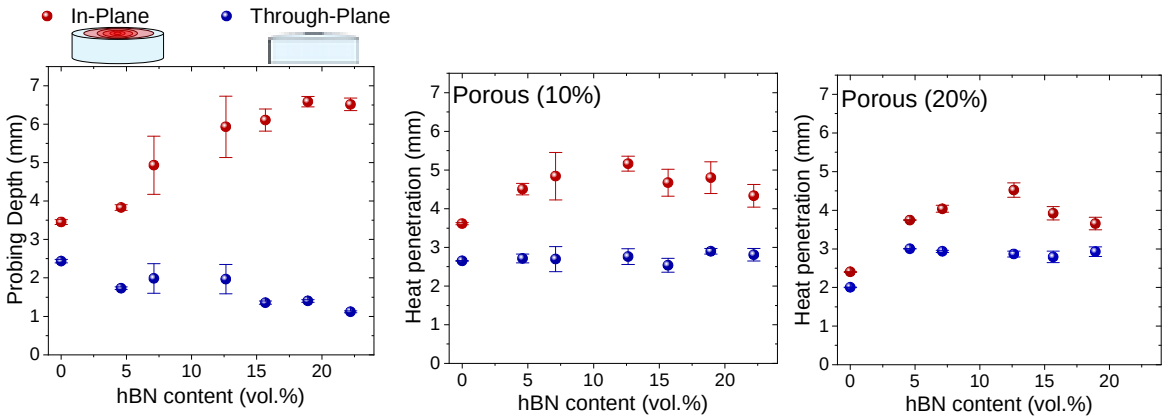

Figure S7. The heat penetration (probing depth) during thermal conductivity measurement using Anisotropic Measurement Module for solid and porous HDPE/hBN composites

References:

(1) Lee, J. W. S.; Wang, J.; Yoon, J. D.; Park, C. B. Strategies to Achieve a Uniform Cell Structure with a High Void Fraction in Advanced Structural Foam Molding. *Ind. Eng. Chem. Res.* **2008**, *47* (23), 9457–9464. https://doi.org/10.1021/ie0707016.

(2) Gustafsson, S. E. Transient Plane Source Techniques for Thermal Conductivity and Thermal Diffusivity Measurements of Solid Materials. *Rev. Sci. Instrum.* **1991**, *62* (3), 797–804. https://doi.org/10.1063/1.1142087.

(3) Gustavsson, M.; Karawacki, E.; Gustafsson, S. E. Thermal Conductivity, Thermal Diffusivity, and Specific Heat of Thin Samples from Transient Measurements with Hot Disk Sensors. *Rev. Sci. Instrum.* **1994**, *65* (12), 3856–3859. https://doi.org/10.1063/1.1145178.

(4) Miller, M. G.; Keith, J. M.; King, J. A.; Edwards, B. J.; Klinkenberg, N.; Schiraldi, D. A. Measuring Thermal Conductivities of Anisotropic Synthetic Graphite-Liquid Crystal Polymer Composites. *Polym. Compos.* **2006**, *27* (4), 388–394. https://doi.org/10.1002/pc.20231.

(5) He, Y. Rapid Thermal Conductivity Measurement with a Hot Disk Sensor: Part 1. Theoretical Considerations. *Thermochim. Acta* **2005**, *436* (1–2), 122–129. https://doi.org/10.1016/j.tca.2005.06.026.